Results in Physics 8 (2018) 336–340

Contents lists available at ScienceDirect

Results in Physics

journal homepage: www.journals.elsevier.com/results-in-physics

Synthesis of Ag and Au nanoparticles embedded in carbon film: Optical, crystalline and topography analysis

Hediyeh Gholamali [a], Azizollah Shafiekhani [b,c,*], Elham Darabi [a], Seyed Mohammad Elahi [a]

[a] Department of Physics, Science and Research Branch, Islamic Azad University, Tehran, Iran
[b] School of Physics, Institute for Research in Fundamental Sciences, P.O. Box 19395-5531, Tehran, Iran
[c] Physics Department, Alzahra University, Vanak, Tehran 1993891167, Iran

ARTICLE INFO

Article history:
Received 16 October 2017
Received in revised form 11 December 2017
Accepted 11 December 2017
Available online 15 December 2017

Keywords:
Ag-DLC
Au-DLC
LSPR
PSD
Crystalline structures

ABSTRACT

Atomic force microscopy (AFM) images give valuable information about surface roughness of thin films based on the results of power spectral density (PSD) through the fast Fourier transform (FFT) algorithms. In the present work, AFM data are studied for silver and gold nanoparticles (Ag NPs a-C: H and Au NPs a-C: H) embedded in amorphous hydrogenated carbon films and co-deposited on glass substrate via of RF-Sputtering and RF-Plasma Enhanced Chemical Vapor Deposition methods. Here, the working gas is acetylene and the targets are Ag and Au. While time and power are constant, the only variable parameter in this study is initial pressure. In addition, the crystalline structure of Ag NPs a-C: H and Au NPs a-C: H are studied using X-ray diffraction (XRD). UV–visible spectrophotometry will also investigate optical properties and localized surface plasmon resonance (LSPR) of samples.

Introduction

Diamond-like Carbon (DLC) films are amorphous carbon (a-C) or hydrogenated amorphous carbon (a-C: H) with special SP hybridization (SP^2 and SP^3) where the ratio of SP^2/SP^3 will affect their properties [1–4]. Optical transparency, high resistivity, high hardness, and chemical stability are only some of their properties that make them unique in sputtering process [5–8]. Despite all mentioned advantages of DLC films, high residual stress and low adhesion will restrict their applications. Embedding monometallic nanoparticles such as Ag, Au and Cu, and bimetallic nanoparticles such as Ag-Au into DLC films will develop their properties and dispel all limitations. The achieved films are widely used in catalysis, optical sensors, and plasmonic devices due to their strong localized surface plasmon resonance [9,10]. Some of the important methods for growing Metal-DLC films are chemical vapor deposition, laser ablation, DC magnetron sputtering, and hybrid deposition system composed of an end-Hall-type hydrocarbon ion gun and metal DC magnetron sputter source.

The effect of nature and substrate structure on physical and chemical properties of microstructure and surface morphology are significant [11–15]. Due to high vertical and spatial resolution, atomic force microscopy (AFM) is an improved tool for micro roughness characterization of a thin film surface via three important factors: Root mean square (RMS) roughness, average roughness, and peak to valley roughness. From spectroscopic aspect, another considerable method for characterizing surface morphology is its frequency distribution which is presented as power spectral density (PSD) technique [7,16–19].

In this work, Ag and Au targets are used independently for preparing Ag-DLC and Au-DLC thin films by co-deposition of RF-sputtering and RF-PECVD method. Reactive gas in plasma RF system is acetylene and deposition process is carried out at room temperature in 60 s with the constant power. The only variable parameter is gas initial pressure. Analyzing the images of the atomic force microscopy (AFM), yields us information about statistical parameters of Ag-DLC and Au-DLC. Moreover, a power spectral density (PSD) plot provides valuable information on spatial frequencies of height distribution.

Experimental details

Ag-DLC and Au-DLC thin films were synthesized by co-deposition of RF-sputtering and RF-PECVD methods with RF power of 100 W. There were two electrodes with different areas which were located 5 cm apart in the chamber. While the smaller electrode with 7.5 cm diameter was applied as a powered electrode, the larger one as anode and the ultra-clean glass placed on it as

* Corresponding author at: School of Physics, Institute for Research in Fundamental Sciences, P.O. Box 19395-5531, Tehran, Iran.
E-mail address: ashafie@ipm.ir (A. Shafiekhani).

https://doi.org/10.1016/j.rinp.2017.12.033
2211-3797/

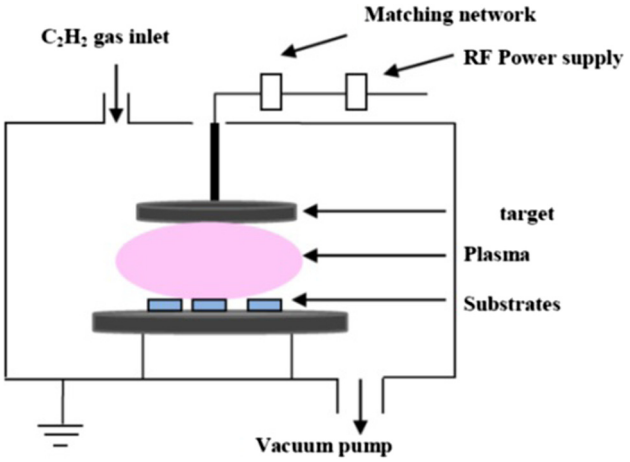

Fig. 1. The schematic of experimental set up.

the substrate. The 60 s deposition process was took place at room temperature. Fig. 1 represents the schematic of the system set up.

Table 1 summarizes the deposition conditions of group A and B with Ag and Au targets respectively, each were synthesized at different initial pressures.

Optical properties of the samples were compared by using UV–vis spectrometer (Stellar-Net, EPP2000). In addition, atomic force microscopy (AFM) with DMC DS 95 series in non-contact mode was used to evaluate feature and topography of the films.

Results and discussion

In order to study the effect of pressure, the power regime was set to be constant (100 W) during 60 s deposition process. Fig. 2 shows the diagram of time deposition (s) versus the initial pressure (pa). It is observed that in the first 20 s, due to high deposition rate of carbon, the pressure dropped dramatically to the critical pressure from 1.75 Pa to 1.90 Pa. Afterwards, the pressure increased slightly and the sputtering process of Ag and Au began. The slow increase of the pressure may be the result of simultaneous deposition of hydrocarbon film, Ag and Au NPs.

Because of higher mobility of electrons in the plasma, a sheath with an excess of ions is created between two electrodes in the plasma region [20] which behave like diodes and the electrodes find dc self-bias voltages. The relation between voltages and the area of electrodes is as follow:

$$\frac{V_1}{V_2} = \left(\frac{A_2}{A_1}\right)^q \quad (1)$$

where V_1 and A_1 are the voltages of the sheath and the area of grounded electrode respectively, and V_2 and A_2 are the related values for the powered electrodes. There are also different reports for the value of q. For instance, in a capacitive divider state and according to electrodes inverse capacitance, q is assumed to be 2 [20]. Considering the collisionless Child-Langmuir law for the sheath dynamic, q becomes 4 [21,22] and finally, q = 2.5 when the sheath dynamics do follow the collisional Child–Langmuir law [22].

Mashayekhi et al. [23] set q = 2.5 by considering a collisional Child–Langmuir law which is much closer to the experimental results. In our system, $\frac{V_1}{V_2}$ was calculated 0.008. Therefore, the sheath voltage of powered electrode is almost the same as bias voltage ($V_{bias} = -(V_1 - V_2)$). Considering the grounded electrode makes the powered electrode become negative [20] and hence, because of negative sheath potential, the positive hydrocarbon radicals are accelerated toward Ag and Au targets. Based on Eq. (2), the bias voltage of plasma depend on RF power (W) and pressure (P) [20]:

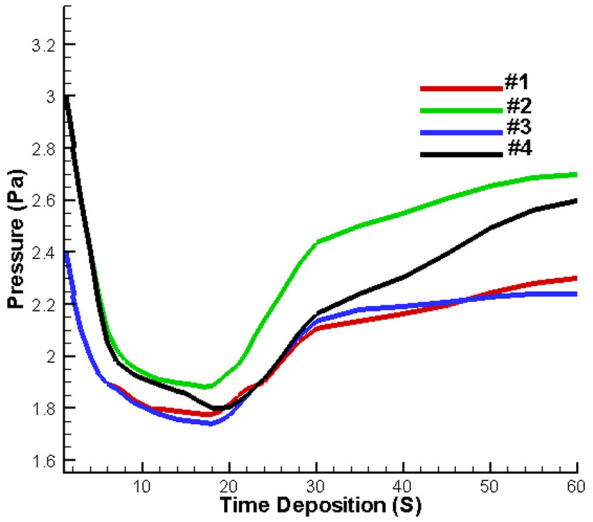

Fig. 2. The monitored pressure during deposition process of all samples.

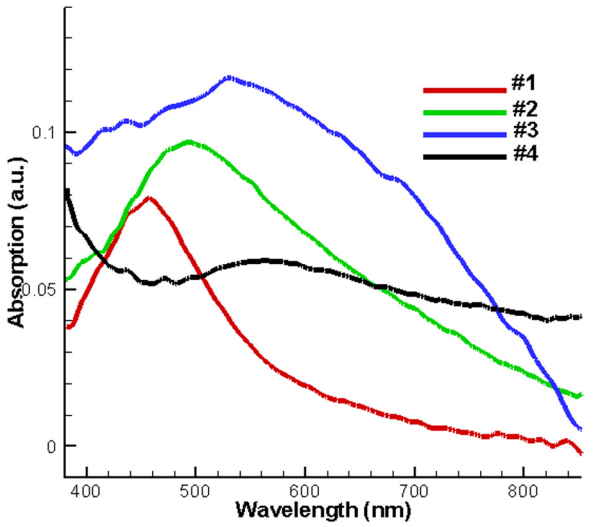

Fig. 3. LSPR of Ag and Au NPs for all samples.

Table 1
The deposition conditions of two groups of samples with Ag and Au targets.

Group	Sample No.	Target	Initial pressure (Pa)	Time deposition (s)	RF power (W)
A	1	Ag	2.4	60	100
A	2	Ag	3	60	100
B	3	Au	2.4	60	100
B	4	Au	3	60	100

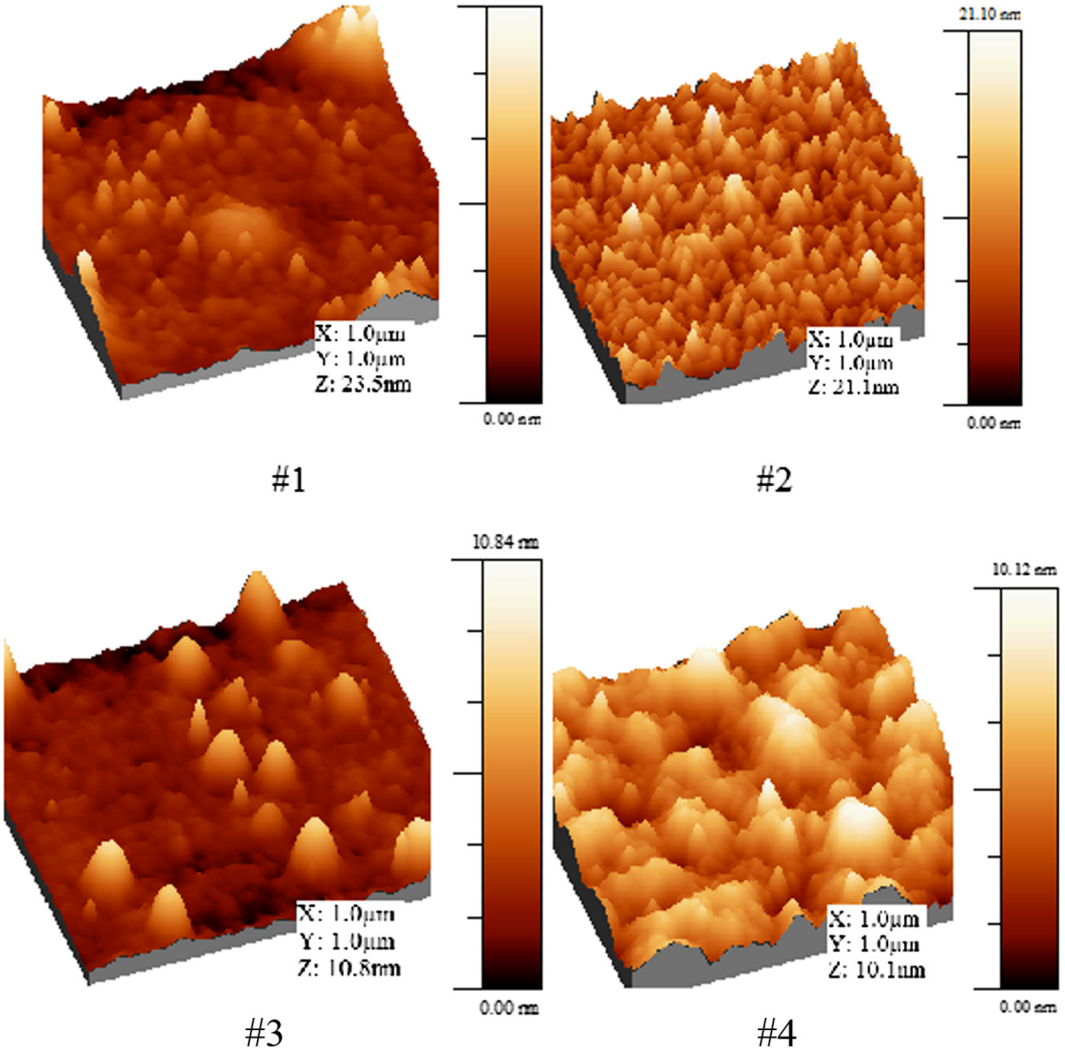

Fig. 4. 1.0 μm × 1.0 μm three dimensional AFM images of all samples.

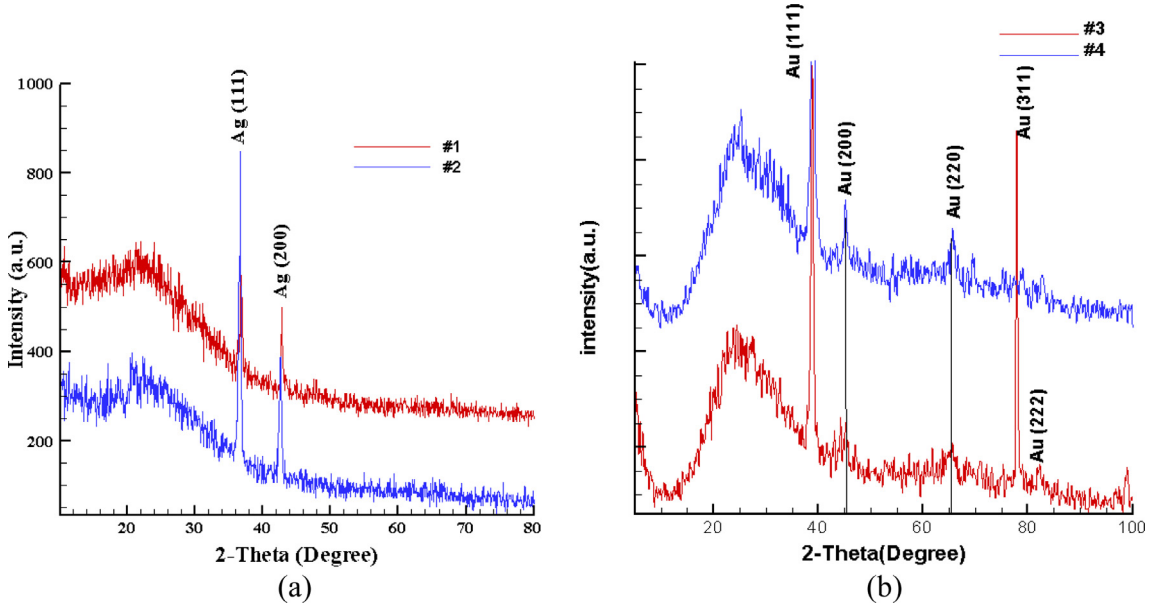

Fig. 5. X-ray diffraction profile of Ag NPs a-C: H and Au NPs a-C: H.

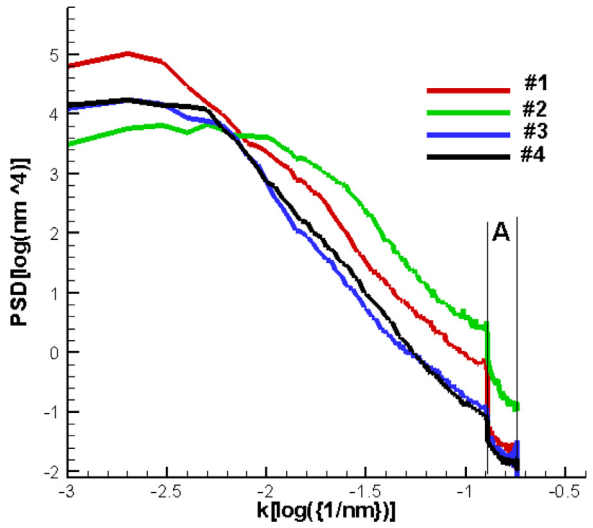

Fig. 6. PSD plots of all samples by FFT algorithm. Part A introduces high frequency region of all samples.

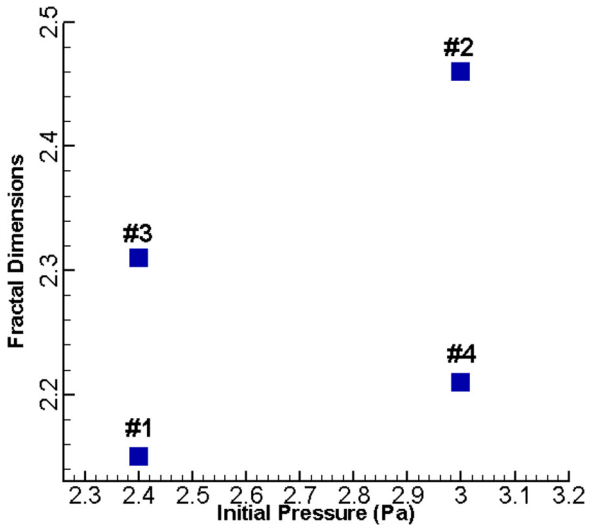

Fig. 8. The dependency fractal dimension to the initial pressure for all specimens.

Table 2
The slope and fractal dimension (D_f) which is obtained from $D_f = 4 + \frac{\beta}{2}$ (Eq. (4)).

Sample No.	Slope	Fractal dimensions (D_f)
#1	−3.70	2.15
#2	−3.08	2.46
#3	−3.38	2.31
#4	−3.59	2.21

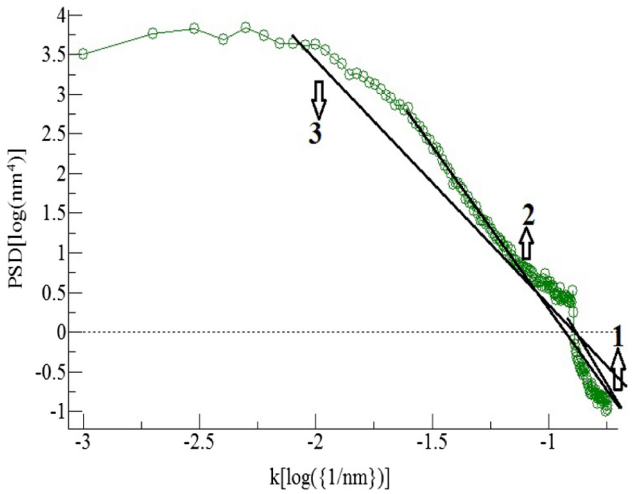

Fig. 7. Typical power spectral density versus frequency (k) showing different slope values in different parts of sample 2.

Table 3
The relation between slopes and fractal dimensions for different frequency region.

Frequency region	Slope	Fractal dimension
High	−5.34	1.33
Mid	−4.18	1.91
Low	−3.08	2.46

$$V_{bias} = k\frac{W}{\sqrt{P}} \tag{2}$$

where k is a constant coefficient. Therefore, in a constant power regime (W), the V_{bias} is increased.

One of the useful criteria for physical and biological properties of metal nanoparticles is localized surface plasmon resonance (LSPR). It is noteworthy to mention that among all types of nanoparticles, powder nanoparticles or colloidal are of great interest due to their applications. Ag and Au nanoparticles should be coated with protective layer in order to avoid fast oxidation which makes the LSPR detection of nanoparticles harder. Therefore, no plasmon would be excited in these materials where the real part of their oxides' permittivity is positive [24,25]. The only way of detecting LSPR is embedding Ag and Au nanoparticles in a transparent and protective environment such as a-C: H.

In Fig. 3, LSPR of Ag and Au NPs create absorption peaks at 470 nm and 550 nm [3,26]. π-$\pi*$ transitions are the origin of absorption peak creation in the UV region. Increasing pressure ends to the increase of the LSPR peak intensity from 0.59 to 1.18 which approve the reduction of absorption coefficient for all samples. This fact is proved by ellipsometric measurements of "k". As a result, the order of LSPR peak intensity represented the order of absorption coefficient of the sample (Fig. 3).

Crystallized Ag and Au NPs of all samples are observed in the XRD profiles of Fig. 5. In Fig. 5a, (1 1 1) and (2 0 0) sharp peaks are related to $2\theta = 36°$ and $2\theta = 42°$ for Ag NPs a-C: H while sharp peaks of (1 1 1) and (3 1 1) in Fig. 5(b) are assigned to $2\theta = 38°$ and $2\theta = 78°$ for Au NPs a-C: H. All mentioned peaks show good crystallinity of prepared Ag and Au NPs. The first wide peak for all peaks is related to the substrate.

PSD plots of each sample are extracted from 1.0 μm × 1.0 μm AFM images (Fig. 4) by FFT algorithm. It can be seen that all PSD plots consist of a plateau in the low spatial frequency area and an inverse slope in high spatial frequency region. These features were characterized with the k-correlation model [27,28] for the auto-covariance function PSD_{ABC} as follow:

$$PSD_{ABC} = \frac{A}{(1 + B^2 f^2)^{\frac{(C+1)}{2}}} \tag{3}$$

where f is spatial frequency and A, B, C are the function parameters. Here, A is the height of the rough surface at low spatial frequency [29], B is the slope of a line connecting two points on the surface which determines the position of the 'knee', and C gives information about nature of roughness at high spatial frequency region with the constant value greater than 2. All curves are almost the same in all frequency range except region A which is specified in Fig. 6. While there is a direct relation between PSD and initial pressure for Ag

sample, an inverse relation exist for Au sample in the frequency range of −0.89 to −0.74.

It is also believed that the majority of the energy exists in the low- and mid-frequency range of the power spectrum which represents the background and large-scale features of an image. However, high-frequency range contains fine and detailed features [30] which make this region more suitable for getting information about surface. From Fig. 6, the shapes of the curves for thin films with different initial pressures are different. Curve changes in high-frequency range reflect the complexity of the very fine structures of the film surface. Another important result is that fractal dimension in region A will increase by reducing the slope [31].

Fractal dimension (D_f) is an important parameter for surface morphology evaluation which are calculated by Eq. (4) and summarized in Table 2. This value determines the relative amounts of the surface irregularities at different distance scales.

The slope variation of power spectral density–frequency (log–log) plot for sample 2 indicate fractal dimension which is shown in Fig. 7. The specified lines 1, 2, and 3 shows the slopes of the desired part which is best fitted in line 3. Thus, the power spectral density method is sensitive to data set size, frequency, and the spectral range [32]. The relationship between slopes and fractal dimensions for different frequency regions are also summarized in Table 3.

In addition, the relationship between the initial pressure and the fractal dimension of thin films is shown in Fig. 8. Increasing fractal dimension will increase initial pressure of the films with Ag nanoparticles and will decrease initial pressure of the thin films with Au nanoparticles. The resistivity is generally changed with the fractal dimension. As the amorphous films are crystalized because of ion bombardment, fractal dimensions of all samples with different percentage of carbon will change and the structure stability will increased.

Conclusion

Ag NPs a-C: H and Au NPs a-C: H thin films were prepared by co-deposition of RF-Sputtering and RF-PECVD methods. During deposition process, silver and gold nanoparticles percentages of thin films were controlled by the initial pressure. The constant parameters in this work were power and time. According to UV–visible absorption spectra, increasing Ag nanoparticles increased the intensity of LSPR peak. However, increasing Au content had an inverse effect. Moreover, fractal and roughness information are extracted from correlation and PSD analysis while the effect of initial pressure on them were studied through FFT algorithm. As it was shown, while initial pressure was increased, PSD and fractal dimension of the surfaces were increased in DLC films with Ag NPs and were decreased in DLC films with Au nanoparticles.

Declaration of interest

The authors report no conflict of interests. The authors alone are responsible for the content and writing of the paper.

References

[1] Ţălu Ş, Bramowicz M, Kulesza S, Shafiekhani A, Ghaderi A, Mashayekhi F, et al. Ind Eng Chem Res 2015;54(33):8212–8.
[2] Ţălu Ş, Bramowicz M, Kulesza S, Shafiekhani A, Rahmati M, Ghaderi A, et al. Surf Interface Anal 2017;49(3):153–60.
[3] Ţălu Ş, Bramowicz M, Kulesza S, Solaymani S, Shafikhani A, Ghaderi A, et al. J Ind Eng Chem 2016;35:158–66.
[4] Ghodselahi T, Vesaghi MA, Gelali A, Zahrabi H, Solaymani S. Appl Surf Sci 2011;258(2):727–31.
[5] Dalouji V, Elahi SM, Solaymani S, Ghaderi A, Elahi H. Appl Phys A 2016;122(5):541.
[6] Dalouji V, Asareh N, Hashemizadeh SA, Solaymani S. Eur Phys J Plus 2016;131(12):442.
[7] Dalouji V, Elahi SM, Ghaderi A, Solaymani S. Chin Phys Lett 2016;33(8):086601.
[8] Ghodselahi T, Solaymani S, Akbarzadeh Pasha M, Vesaghi MA. Eur Phys J D 2012;66:299.
[9] Ghodselahi T, Neishaboorynejad T, Arsalani S. Appl Surf Sci 2015;343:194–201.
[10] Ţălu S, Stach S, Ghodselahi T, Ghaderi A, Solaymani S, Boochani A, et al. J Phys Chem B 2015;119(17):5662–70.
[11] Molamohammadi M, Luna C, Arman A, Solaymani S, Boochani A, Ahmadpourian A, et al. J Mater Sci Mater Electron 2015;26(9):6814–8.
[12] Solaymani S, Ghaderi A, Beryani Nezafat N. J Fusion Energy 2012;31(6). 591 591.
[13] Ţălu Ş, Bramowicz M, Kulesza S, Ghaderi A, Dalouji V, Solaymani S, et al. J. Microsc. 2016;264(2):143–52.
[14] Dejam L, Elahi SM, Nazari HH, Elahi H, Solaymani S, Ghaderi A. J Mater Sci Mater Electron 2016;27:685–96.
[15] Ţălu Ş, Solaymani S, Bramowicz M, Kulesza S, Ghaderi A, Shahpouri S, et al. J Mater Sci Mater Electron 2016;27(9):9272–7.
[16] Solaymani S, Elahi SM, Nezafat NB, Zahrabi H, Boochani A, Naseri M. Eur Phys J Appl Phys 2013;64:11301.
[17] Ţălu Ş, Bramowicz M, Kulesza S, Ghaderi A, Solaymani S, Savaloni H, et al. J Ind Eng Chem 2016;43:164–9.
[18] Naseri N, Solaymani S, Ghaderi A, Bramowicz M, Kulesza S, Ţălu Ş, et al. RSC Adv 2017;7(21):12923–30.
[19] Dalouji V, Elahi SM, Ghaderi A, Solaymani S. Chin Phys Lett 2016;33(5):057203.
[20] Robertson J. Mater Sci Eng R 2002;37:129.
[21] Ohering M. Materials science of thin films deposition and structure. 2nd ed. San Diego: Academic Press; 2002. p. 215.
[22] Lieberman MA, Lichteberg AJ. Principles of plasma discharges and materials processing. 2nd ed. Hoboken, New Jersey: John Wiley & Sons Inc; 2005. p. 430–2.
[23] Mashayekhi F, Shafiekhani A, Sebt SA. Eur Phys J Appl Phys 2016;74:30402.
[24] Sokolik N, Toon OB. J Geophys Res 1999;104:9423.
[25] Schlegel A, Alvarado SF, Wachter P. J Phys C 1979;12:1157.
[26] Naderi S, Ghaderi A, Solaymani S, Golzan MM. Eur Phys J Appl Phys 2012;58(2):377.
[27] Sahoo NK, Thakur S, Tokas RB. Thin Solid Films 2006;503:85–95.
[28] Senthilkumar M, Sahoo NK, Thakur S, Tokas RB. Appl Surf Sci 2005;252:1608–19.
[29] Singh JP, Singh R, Mishra NC, Kanjilal D, Ganesan V. J Appl Phys 2001;90(12):5968–72.
[30] Castleman KR. Digital image processing. New Jersey: Prentice Hall; 1996. p. 207.
[31] Wang Y, Xu K-W. Appl Surf Sci 2010;256:2915–9.
[32] Tayfun B, Kayhan D. Fractal 2001;9:105.